

1   **Title:** APNet, an explainable sparse deep learning model to discover differentially active drivers of  
2   severe COVID-19

3   **Authors:** George I. Gavriilidis<sup>1</sup>, Vasileios Vasileiou<sup>1,2</sup>, Stella Dimitsaki<sup>1</sup>, George Karakatsoulis<sup>1</sup>,  
4   Antonis Giannakakis<sup>2,3</sup>, Georgios A. Pavlopoulos<sup>4,5</sup>, Fotis Psomopoulos<sup>1</sup>

5

6   <sup>1</sup>Institute of Applied Biosciences, Centre for Research and Technology Hellas, Thessaloniki, Greece

7   <sup>2</sup>Department of Molecular Biology and Genetics, Democritus University of Thrace, Alexandroupolis, Greece

8   <sup>3</sup>University Research Institute of Maternal and Child Health and Precision Medicine, National and Kapodistrian University of Athens, 11527  
9   Athens, Greece

10   <sup>4</sup>Institute for Fundamental Biomedical Research, BSRC “Alexander Fleming”, Vari, Greece

11   <sup>5</sup>Center of New Biotechnologies & Precision Medicine, Department of Medicine, School of Health Sciences, National and Kapodistrian  
12   University of Athens, Athens, Greece

13

14

15

16

17

18   \*Corresponding author: George I. Gavriilidis

19   Email: [ggeorav@certh.gr](mailto:ggeorav@certh.gr)

20

21   **Keywords:** SJARACNe, NetBID2, COVID-19, SARS-CoV-2, proteomics, Olink, scMINER, Deep  
22   Learning, PASNet, Explainable AI

23

24

25

26 **Abstract**

27 **Motivation:** Computational analyses of plasma proteomics provide translational insights into complex  
28 diseases such as COVID-19 by revealing molecules, cellular phenotypes, and signaling patterns that  
29 contribute to unfavorable clinical outcomes. Current *in silico* approaches dovetail differential  
30 expression, biostatistics, and machine learning, but often overlook nonlinear proteomic dynamics, like  
31 post-translational modifications, and provide limited biological interpretability beyond feature ranking.

32 **Results:** We introduce APNet, a novel computational pipeline that combines differential activity  
33 analysis based on SJARACNe co-expression networks with PASNet, a biologically-informed sparse  
34 deep learning model to perform explainable predictions for COVID-19 severity. The APNet driver-  
35 pathway network ingests co-expression and classification weights to aid result interpretation and  
36 hypothesis generation. APNet outperforms alternative models in patient classification across three  
37 COVID-19 proteomic datasets, identifying predictive drivers and pathways, including some confirmed  
38 in single-cell omics and highlighting under-explored biomarker circuitries in COVID-19.

39 **Availability and Implementation:** APNet's R, Python scripts and Cytoscape methodologies are  
40 available at <https://github.com/BiodataAnalysisGroup/APNet>

41 **Contact:** [ggeorav@certh.gr](mailto:ggeorav@certh.gr)

42 **Supplementary information:** Supplementary information can be accessed in Zenodo  
43 (10.5281/zenodo.10438830).

44

45 **Abbreviations**

46 APNet Activity PASNet

47 ARDS Acute Respiratory Distress Syndrome

48 AUC Area Under the Curve

49 DAPs Differential Active Proteins

50 DEPs Differential Expressed Proteins

51 DL Deep Learning

52 DOME Data, Optimization, Model, Evaluation

53 EXP Expression Values

54 ICU Intensive Care Unit

55 KG Knowledge Graph

56 Mayo Mayo Clinic

57 MGH Massachusetts General Hospital

58 MI Mutual Information

59 MLP Multi-Layer Perceptron

60 NPX Normalized Protein eXpression

61 PASNet Pathway-Associated Sparse Deep Neural Network

62 PBMC Peripheral Blood Mononuclear Cell

63 PEA Proximity Extension Assay

64 RF Random Forest

65 ROC Receiver Operating Characteristic

66 SFA Signal Flow Analysis

67 SHAP Shapley additive explanation

68 Stanford Stanford Hospital

69 SVM Support Vector Machine

70 WHO World Health Organization

71 XAI eXplainable Artificial Intelligent

72

73

74

## 1. Introduction

75 Human plasma is a vital clinical specimen encompassing a broad spectrum of proteins, including tissue  
76 markers, immunoglobulins, transcription factors, kinases, metabolites, and secreted factors (Eldjarn et  
77 al., 2023; Zhong et al., 2021). With the advent of high-throughput technologies (-omics), the human  
78 plasma proteome has become a focal point for discovering novel biomarkers and therapeutic targets for  
79 complex diseases. This has been especially the cases with severe COVID-19, a condition besetting  
80 many patients infected with the SARS-CoV-2 coronavirus (Babačić et al., 2023). Plasma proteomics  
81 have provided significant biological insights into the immunopathology of severe COVID-19, which is  
82 characterized by the inflammatory "cytokine storm", Acute Respiratory Distress Syndrome (ARDS),  
83 PANoptosis-induced cell death, and multiorgan failure (Diamond and Kanneganti, 2022). Plasma  
84 proteomics has also been explored in long-COVID-19 syndromes and vaccine response variations  
85 (Liang et al., 2023).

86 Many studies have measured plasma proteomics using Olink Proximity Extension Assay (PEA) in  
87 COVID-19 research due to this technology's specificity, scalability and multiplexing benefits (Wik et  
88 al., 2021). In our recent work, we assessed pertinent Machine Learning models applied in these high-  
89 dimensional datasets like Random Forest, Gradient Boosted Decision Tree, XGBoost, Extra Tree  
90 classifiers, Logistic regression, Lasso Logistic regression, Support Vector Machine (SVM), and Deep  
91 Learning (DL) (e.g., AutoGluon-Tabular). Some models exhibited eXplainable AI (XAI) features by  
92 deploying Shapley additive explanation (SHAP) values, the minimal-optimal variables method or a  
93 random forest explainer. In the same work, we managed to dovetail an explainable, computational  
94 pipeline to benchmark a wide assortment of ML tools on predicting COVID-19 severity from Olink  
95 plasma proteomics which revealed Multi-Layer Perceptron (MLP) as the highest-performing algorithm  
96 (Dimitsaki et al., 2023).

97 However, most of the above studies can partially approximate proteomic non-linear dynamics (e.g.,  
98 post-translational modifications, protein co-expression networks, complex formation, and subcellular  
99 localization), thus missing signaling proteins that may drive critical COVID-19 pathways. Moreover,  
100 these studies' ML/DL findings often lack extensive external validation in large independent datasets,  
101 while their biological explainability is usually restricted to mere feature ranking (Paul et al., 2023)  
102 (Dimitsaki et al., 2023).

103 Acknowledging these challenges, we introduce Activity PASNet (APNet) in this manuscript. This  
104 computational DL pipeline initially uses the SJARACNe data-driven network algorithms to uncover  
105 disease drivers prioritized based on "activity," an aggregate metric of their capacity to regulate their  
106 transcriptional targets non-linearly (Ding et al., n.d.; Dong et al., 2023). These drivers can be overt  
107 (differentially expressed and possibly active) or "hidden" (differentially active but not expressed). Next,  
108 APNet feeds these drivers into Pathway-Associated Sparse Deep Neural Network (PASNet) (Hao et  
109 al., 2018), which incorporates biological priors as hidden layers to ultimately deliver interpretable

110 clinical classifications, validated by the eXplainable AI component of SHAP values. Finally, APNet  
111 facilitates the analysis of SJARACNe co-expression networks, equipped with the weights from the DL  
112 classification task, to streamline data exploration and the formation of mechanistic hypotheses for  
113 further biological investigation.

114 We extensively trained, tested, and validated APNet on activity matrices from 3 distinct Olink plasma  
115 proteomic datasets (MGH, Mayo, Stanford) (Byeon et al., 2022; Feyaerts et al., 2022; Filbin et al.,  
116 2021). APNet managed to pinpoint ground-truth drivers of severity, predicted new proteomic markers  
117 with potential theranostic potential (some of which were traced to circulating PBMCs through scRNA-  
118 seq analysis), outperformed alternative ML/DL models in demarcating severe COVID-19 cases and  
119 enabled the inference of a potential signaling network from predictive factors in the liver of individuals  
120 with severe COVID-19.

121

122 **2. Materials and methods**

123 **2.1 APNet overview**

124 APNet is a modular pipeline (Figure 1) which aims to facilitate the discovery of novel predictive drivers  
125 of severe clinical outcomes and to facilitate the formulation of mechanistic hypotheses. In this present  
126 work, we considered cases experiencing severe and non-severe COVID-19.

127

128 **2.2 Brief description of APNet modular architecture**

129 **2.2.1 Module 1- Differential activity analysis for drivers of COVID-19 severity**

130 In this module, conversions of expression values to activity values for plasma proteomics were  
131 accomplished with NetBID2 (Dong et al., 2023) toolkit whereas for scRNA-seq data with scMINER  
132 toolkit (Ding et al., 2023). For the plasma proteomics, we applied the NetBID2 algorithm, which  
133 reverse-engineers context-specific interactomes and integrates network activity inferred from large-  
134 scale multi-omics data, empowering the identification of hidden drivers that traditional analyses cannot  
135 detect. By leveraging the MSigDB database, we compiled distinct lists of Transcription Factors (TF)  
136 and signaling molecule proteins. Separate TF and signaling molecule networks were constructed using  
137 SJARACNe. These networks featured drivers (hubs) connected to their targets through protein-protein  
138 interactions, derived from their expression patterns.

139 To calculate the activities of driver proteins in each dataset based on protein expression, we employed  
140 the "cal.Activity" function in NetBID2. The weighted mean activity of a driver candidate protein  
141 (Driver $\{i\}$ ) in sample s, was computed using the following equation:

$$142 \quad Driver_{si} = \frac{\sum_{j=1}^n SIGN_{ij} * MI_{ij} * EXP_{sj}}{n}$$

143 Here, the NPX count proteomics matrix, EXP $\{sj\}$  represented the expression value of gene j in sample  
144 s, MI $\{ij\}$  indicated the mutual information between master regulator protein i and its target protein j,  
145 and SIGN $\{ij\}$  was the sign of the Spearman correlation between protein i and its target protein j. The  
146 total number of targets for DRIVER i was denoted by n.

147 Differential activities were then computed for Severe and Non-Severe Status across the three datasets,  
148 by using the "getDE.BID.2G" function, allowing us to identify genes exhibiting distinct regulatory  
149 patterns in response to severity variations, through Bayesian model.

150 Also, we deployed the scMINER workflow, based also on SJARACNe, to discover severity drivers in  
151 MGH scRNAseq data. For both differential expression and differential activity, the function get.DA  
152 was performed by using the SCT matrix and activity matrix, respectively. Data visualisation for single-  
153 cell analysis was performed through the Seurat pipeline (4.3.0).

154 **2.2.2 Module 2- Driver-pathway mapping**

155 To prepare input data for the biologically explainable PASNet DL model on Module 3, joint  
156 differentially active drivers of severity from the three Olink studies were mapped to biological pathways  
157 using the Enrichr KG (Evangelista et al., 2023). 30 pathways from each of the following resources were  
158 leveraged (KEGG, Reactome, GO:BP and Wikipathways 2021) for the commonly decreased and  
159 increased drivers of severity separately. Drivers were mapped to the retrieved pathways in a binary  
160 fashion with 0s and 1s, i.e. when a driver was participating in the gene set of a pathway it was assigned  
161 the value of 1 and vice versa.

162 **2.2.3 Module 3-Deep Learning classification of Severe COVID-19 cases with biological**  
163 **explainability**

164 The findings from Modules 1 and 2 served as input for Module 3, where a sparse neural network model  
165 called PASNet was used to predict COVID-19 severity. The model was trained on MGH data, validated  
166 on Mayo and tested on Mayo and Stanford datasets. A separate model was trained and tested using  
167 scMGH data. Model performance was evaluated using Area Under the Curve (AUC) and F1-scores,

168 along with ROC curve analysis. The PASNet training phase is expressed through the following  
169 equations.

170 Sparsity of the PASNet sub-network function:  $h^{(l+1)} = a((W^{(l)} * M^{(l)})h^{(l)} + b^{(l)})$

171 
$$M^{(l)} = \{I(|W^{(l)}| \geq Q^{(l)}), \text{if } l \neq 0$$

172 
$$M^{(l)} = \{A, \text{if } l = 0\}$$

173 where

174  $Q^{(l)}$  is the S-th percentile of  $|W^{(l)}|$  if  $l \neq 0$

175 M: mask matrix for each layer

176  $l$ :layer

177 W: weight matrix

178 b: vias vector

179 Cost-sensitive learning for imbalanced data:  $L = \sum_{k=1}^K C_k + \frac{1}{2}\lambda\|W\|_2$

180 
$$C_k = \frac{1}{n_k} \sum_{i=1}^{n_k} c(y_i, \underline{y}_i)$$

181 Thus, the weights and biases on the  $l$ -th layer are updated by:

191 
$$W^{(l)} \leftarrow (I - \eta\lambda)W^{(l)} - \eta \sum_{k=1}^K \frac{dC_k}{dW^{(l)}}$$

192 
$$b^{(l)} \leftarrow b^{(l)} - \eta \sum_{k=1}^K \frac{dC_k}{db^{(l)}}$$

182 where

183  $C_k$ :mean error on the class k

184  $y_i$ :ground truth

185  $\underline{y}_i$ :prediction

186  $n_k$ :number of samples in the class k

187  $L$ : total cost

188  $c(\cdot)$ :cost function (e.g., cross-entropy loss)

189  $\lambda$ : regularization hyperparameter

190  $\eta$ :learning rate

193 Biological explainability of the whole sparse DL model is predicated in the combination of Shapley  
194 values (SHAP) and the driver-pathway mappings that PASNet architecture offers, assigning learning  
195 weights.

$$196 \quad \varphi_i = \sum_{S \in N \setminus \{i\}} \frac{|S|! (M - |S| - 1)!}{M!} [f(S \cup \{i\}) - f(S)]$$

197  $N$ : is the set of all input features

198  $i$ : feature

199  $f$ : model

200  $M$ : is the number of features

201

#### 202 2.2.4 Module 4- Bipartite graph analysis

203 This final APNet module leverages the SJARACNe co-expression networks from each study for the  
204 joint differential active drivers and augments it by connecting drivers to pathways based on Module 2.  
205 The weights of driver-driver edges contain the Mutual Information (MI) metric and the Spearman  
206 correlation coefficient (positive values signify activation, negative values the opposite), amongst other  
207 metrics. Driver-pathway edges contain as weights the PASNet-weights that PASNet learned during  
208 training-testing tasks from Module 3. Our study used Cytoscape to perform network visualization, basic  
209 analysis for network statistics and centrality metrics (Betweenness Centrality algorithm),  
210 dimensionality reduction using tSNE (cluster signal propagation simulation (OCSANA+) and analysis  
211 for shortest paths (PathLinker tool)(Gil et al., 2017; Marazzi et al., 2020).

212 OCSANA+ is a Cytoscape application that analyses the structure of large-scale complex networks. It  
213 identifies nodes that drive the system towards a desired long-term behavior and ranks the combinations  
214 of interventions that are likely to be more effective. Additionally, it estimates the effects of perturbations  
215 in signaling networks. We used the Signal Flow Analysis (SFA) feature of OCSANA+ to simulate  
216 signal propagation. The SFA algorithm estimates the signal flow in a signaling network by analyzing  
217 the topological information. It employs a linear difference equation that considers a node's previous  
218 activity, the effect and influence of incoming edges, and the initial activities of the node. The algorithm  
219 focuses on the information conveyed by a series of biological interactions represented in a signaling  
220 network (Marazzi et al., 2020).

221 PathLinker is a Cytoscape app based on an algorithm reconstructing interactions in a signaling pathway.  
222 It requires a directed network, a set of sources, and a set of targets as inputs. The algorithm computes  
223 the k best-scoring loopless paths and outputs the sub-network of the k best paths. The algorithm offers

224 three choices for managing edge weights: (i) No weights: Path score is based solely on the number of  
225 edges in the path, and PathLinker identifies the k paths with the lowest scores, (ii) Additive edge  
226 weights: Path score results from the summation of edge weights, and PathLinker finds the k paths with  
227 the lowest scores in this scenario as well, (iii) Probabilistic edge weights: Common in protein interaction  
228 networks, where weight represents experimental reliability. PathLinker treats these weights as  
229 multiplicative, seeking the k paths with the highest cost, where the product of edge weights determines  
230 cost. Internally, PathLinker transforms each weight by taking the absolute value of its logarithm to map  
231 the problem to the additive case (Gil et al., 2017) (Figure 2).

232

### 233 **2.3 Technical benchmarking and bioinformatic validation based on COVID-19 prior knowledge**

234 To benchmark APNet's performance on patient classification from Olink plasma proteomics, we  
235 deployed the PASNet approach on original NPX values of Olink plasma proteomics and a Random  
236 Forest model on the transformed activity values. Firstly, for PASNet we used the expression values for  
237 training, validation and test, by using the count matrices of MGH, Mayo and Stanford, respectively.  
238 The count matrices were filtered by keeping only the common significant proteins across 3 datasets  
239 from Differential Expression analysis to perform the PASNet approach on expression data. Similarly to  
240 the APNet approach, pathways collected from EnrichR-KG, by using (KEGG, Reactome, GO:BP and  
241 Wikipathways 2021) for the commonly decreased and increased drivers of severity separately. PASNet  
242 used the count matrices across 3 datasets for training, validation, and test, by using MGH, Mayo, and  
243 Stanford respectively. Then for Random Forest, we used activity matrices from 3 datasets, by applying  
244 training, validation and test into MGH, Mayo and Staford, respectively.

245 Bioinformatic validation of the top 20 most predictive drivers for each experiment was pursued by  
246 mapping these drivers to the 9 curated networks regarding COVID-19 immunopathological hallmarks  
247 by SIGNOR (<https://signor.uniroma2.it/covid/>). Level 4 networks were obtained for each COVID-19  
248 hallmarks and downstream processing was conducted in Cytoscape.

249 Finally, selective data mining for key drivers of interest was performed in the web tool  
250 <https://www.covid19dataportal.org/>.

251

### 252 **2.4 DOME recommendations**

253 The assembly of APNet was performed considering the recently published DOME recommendations,  
254 a set of community-wide recommendations for reporting supervised machine learning-based analyses

255 applied to biological studies (see supplementary information) (Walsh et al., 2021) (Supplementary  
256 Material 1).

257

258 **3. Results**

259 **3.1 Harmonization of COVID-19 patient cohorts and assembly of plasma proteomic datasets**

260 Initially, we harmonized patient stratification for COVID-19 severity based on WHOscore (“Severe”  
261 vs “NonSevere”) across the three Olink proteomic datasets. In particular, COVID-19 cases who had a  
262 fatal outcome or were admitted in the ICU or were intubated were designated as “severe” and the  
263 residual cases were designated as “non-severe”. In the MGH study, we designated 80 severe and 225  
264 non-severe cases. In the Mayo study, we demarcated 268 severe and 181 non-severe COVID-19 cases.  
265 Furthermore, we determined 24 severe and 40 non-severe cases in the Stanford study. Associations with  
266 respective WHOscores and age can be seen in (Sup. Figure 1).

267 From all 3 Olink studies, 1463 common plasma proteins were bioinformatically studied within APNet  
268 and were used for downstream processing to uncover predictive markers of severity.

269

270 **3.2 Data preprocessing and detection of severity drivers across proteomic studies**

271 Next, we used the NetBID2 toolkit through APNet to detect common differentially active proteins  
272 (DAPs) in severe COVID-19 cases, for all three Olink studies. Notably, for MGH, the prominent  
273 positive drivers included TACSTD2, BAG3, POLR2F, DPY30, and CAPG. Conversely, the top  
274 negative drivers for MGH were CCL22, BTC, IGFBP3, TNFSF11, and ICOSLG (Sup. Figure 2A).  
275 Similarly, in the case of Mayo, the leading positive drivers consisted of VSIG4, IL1RL1, IL27, KRT19,  
276 and JUN, while negative drivers entailed CDON, CD1C, ITGB7, TNFSF11, and LRRN1 (Sup. Figure  
277 2B). For Stanford, the primary positive drivers were LGALS1, CSTB, MAD1L1, DDAH1, and CCL7  
278 and the negative were EPCAM, CPA2, CDNF, DSG4, and CD1C. Pathway enrichment showed that  
279 these severe COVID-19 top-drivers were associated with cell migration, monocyte activation,  
280 methylation changes and immune cell dysregulation (Sup. Figure 2A-C).

281 From hereon, we focused on the commonly perturbed drivers across the three studies. APNet captured  
282 333 common differentially active proteins (DAPs) across the three studies and encompassed 163  
283 differentially expressed proteins (DEPs) and 170 hidden drivers (i.e., hidden in at least one of the three  
284 Olink datasets) (Figure 3A-B). Among the 333 common drivers, 150 were differentially hyper-active  
285 and 183 were hypo-active in severe COVID-19. When analyzing the STRINGdb network of common

286 DAPs, centrality analysis prioritized DEPs like immuno-regulatory interleukins IL4-IL6, keratin  
287 modulators (KRT19), chemokines for macrophages and neutrophils (CXCL8/CCL20) and transcription  
288 factors (JUN). Other central decreased DEPs were effectors of T cell activation and proliferation  
289 (CD8A, CD28), mediators of developmental pathways like the SCF/c-Kit pathway  
290 (KIT/KITLG/IL7R/FLT3/CD34) and cellular adhesion surface molecules (ITGB1). Similarly, central  
291 hyper-active hidden drivers (“positive”) pertained to growth factors (HGF), ECM remodelers  
292 (metalloprotease inhibitor TIMP1), chemoattractants of monocytes, natural killer and T-cells  
293 (CXCL9/CXCL10/CCL3) and biomarkers of systemic organ failure (the lipocalin LCN2 indicating  
294 acute kidney injury). Other central hypo-active hidden drivers included cellular adhesion molecules  
295 (NCAM1, ITGB2, ITGAV), growth factors (FLT3LG, ligand for the FLT3 receptor found in DEPs) or  
296 cognate receptors (EGFR, receptor for the Epidermal Growth Factor) and the tumour suppressor  
297 molecule PTEN (Figure 3C).

298 Pathway enrichment through the Enrichr KG (KEGG, Wikipathways, Reactome, GO:BP) highlighted  
299 several biological ground truths involved in COVID-19 immunopathology such as increased activation  
300 of innate immunity, lung fibrosis, MAPK signaling, Sars-CoV-2 immuno-evasion, neutrophil  
301 degranulation and viral protein interaction with cytokines and cognate receptors (Figure 3D).  
302 Conversely, dwindling pathways in severe COVID-19 included the hematopoietic system, inhibitors of  
303 the PI3K-Akt signaling pathway, cellular adhesion mechanisms through integrins and the Hippo-Merlin  
304 signaling pathway, revealing an impairment of physiological proliferation and migration for circulating  
305 immune cells (Figure 3E).

306 To better dissect the increased perturbational space captured by APNet, distinct cellular enrichment for  
307 DEPs and hidden drivers was conducted using the GTEx\_Tissues database through Enrichr. DEPs  
308 exhibited an over-representation for peripheral blood, spleen, liver, brain, and adipose tissue. Hidden  
309 drivers, conversely, implicated other organs like oesophagus, tibial nerve and the cardio-vascular  
310 system (Sup. Figure 3A-D). Ensuing pathway enrichment with WikiPathways and GO:BP uncovered  
311 an expected affiliation of DEPs with key COVID-19 molecular “landmarks” like apoptosis, viral life  
312 cycle, neutrophil degranulation, PI3K Akt signaling and impediments in synapse functionality and  
313 angiogenesis. Interestingly, the hidden drivers were skewed towards aberrant insulin signaling, cellular  
314 adhesion imbalances (L1cam interactions), propagation of hypoxia and abnormal neuronal behaviour  
315 (increased neuroinflammation, decreased neuroplasticity) (Sup. Figure 3E-F, Sup. Figure 4).

316 These preliminary findings underline the importance of employing activity transformations on distinct  
317 COVID-19 plasma proteomic datasets using APNet. Beyond mere differential expression, this approach  
318 identified shared, systemic damages caused by Sars-CoV-2 across multiple organs and tissues  
319 (Supplementary Material 2-3).

320 **3.3 APNet classifies severe COVID-19 cases among distinct plasma proteomic studies**

321 At this point, we hypothesized that the newly discovered hidden drivers had untapped biological  
322 potential, which could enhance the clinical prediction of severe COVID-19 cases from plasma  
323 proteomics.

324 We used the common DAPs across the three Olink studies for the ensuing clinical predictions. After  
325 initial training in the MGH dataset (for details, see Materials and Methods), APNet accurately predicted  
326 severe COVID-19 patients during the early testing phase (MGH-Mayo experiment) with significant  
327 robustness (AUC = 0.96, F1 score = 0.9). Biological explainability highlighted the prognostic  
328 significance of various DEPs (JUN, IL6, MAPK9, TNFRSF1A, AREG, NTF4, NCF2, TNFRSF10A,  
329 FLT3, CKAP4, FLT3LG, SDC1, TNFRSF10B, TNFSF11) but also several hidden drivers (FTL3LG,  
330 LYN, PTEN, EFNA1, ACAA1, HGF, TIMP1) (top-20). The most predictive pathways involved the  
331 ground-truth “cytokine storm”, MAPK signaling, vascular damage reflected on atherosclerosis  
332 potential, protein folding (through HSP90 chaperone), and PI3K-Akt signaling pathway (Figure 4A-B).

333 During the second testing phase (MGH-Stanford experiment), APNet once again exhibited significant  
334 predictive robustness since, on the Stanford dataset, it could foreshadow severe COVID-19 efficiently  
335 (AUC = 0.91, F1 score = 0.68). Biological explainability revealed predictive drivers of severity, many  
336 of which overlapped with the ones from the previous testing experiment (i.e. PTEN, JUN, IL6, LYN,  
337 TNFRSF1A, TNFRSF10A, TNFRSF10B, TNFSF10) but also unveiled novel ones (BAX, LTA, KDR,  
338 COL1A1, CCL7, EGFR, ERBB2, CCL22, PODXL, SEMA4D, KIT, ROBO1). The hidden drivers were  
339 PTEN, BAX, CCL22, EGFR, LYN, ROBO1 (Figure 4C).

340 The most predictive pathways in this experiment involved viral infection and disruption of cytokines  
341 and cognate receptors, PI3K-Akt signaling pathway, MAPK signaling, Hippo-Merlin signaling  
342 dysregulation, and intensified Interleukin signaling pathway, apoptotic TRAIL signaling, neurotoxicity  
343 concerning axonogenesis, and imbalances in lipid metabolism (Figure 4D) (Supplementary Material 4).

344 Hierarchical clustering on all cases across studies revealed associations of the most predictive drivers  
345 with COVID-19 severity, while in the MGH study, further associations with diabetes and kidney disease  
346 were also uncovered (Figure 4E).

347

348 **3.4 APNet bridges plasma proteomics with single-cell transcriptomics**

349 At this point, we decided to use APNet for a joint analysis between bulk plasma proteomics (MGH  
350 dataset) and scRNA-seq data from circulating peripheral blood mononuclear cells (PBMCs, 4 severe  
351 and 10 non-severe MGH cases). We sought to (a) prioritize which predictive drivers of COVID-19

352 severity could be important for both -omic modalities and (b) trace the cellular origin of various  
353 predictive drivers of COVID-19 severity from all the insofar classification experiments among the  
354 PBMC cellular populations. (Figure 5A).

355 Initially, we deployed the scMINER toolkit to convert the typical sparse scRNA-seq expression matrix  
356 into a non-sparse activity matrix based on the SJARACNe/MICA/MINIE algorithms (see Materials and  
357 Methods for details). Single-cell differential activity analysis revealed 282 differentially active drivers  
358 (140 DEGs and 142 hidden drivers) in severe COVID-19, which were also perturbed in the MGH  
359 plasma proteomic analysis (Sup. Figure 5A). STRINGdb PPI network modeling and pathway  
360 enrichment implicated several key COVID-19 severity drivers in innate/adaptive immunity, viral  
361 replication, inflammatory signaling, cell adhesion and lipid metabolism (e.g., *IL6*, *NCAM*, *LYN*, *PTEN*,  
362 *ITGB1*, *ITGAM*) (Sup. Figure 5B-D), in line with our findings from the previous plasma proteomic  
363 analyses.

364 Next, we trained APNet on the MGH plasma proteomic dataset and tested it on the MGH single-cell  
365 dataset (scMGH). APNet was highly robust in classifying severe COVID-19 cases (AUC: 0.99, F1-  
366 score: 0.975). The driver-pathway heatmaps pointed towards expected inflammatory and immune  
367 pathways (e.g., IL18 signaling, TLR4 stimulation, T cell differentiation) as predictive signalling motifs  
368 of severe COVID-19. Five predictive drivers from the previous plasma proteomic experiments were  
369 found as predictive genes (*MAPK9*, *TIMP1*, *JUN*, *IL6*, *TNFSF10*). The other multi-omic predictive  
370 drivers were *S100A12*, *CD63*, *LAMP2*, *BIRC2*, *HMOX1*, *LGALS1*, *NFATC1*, *IL10RA*, *ATP6AP2*, *CD4*,  
371 *ITGB1* (Figure 5B-C).

372 Lastly, we probed for the single-cell activity profile of various predictive drivers from the MGH-  
373 Mayo/MGH-Stanford/MGH-scMGH experiments. We discovered that the most active drivers in severe  
374 cases were *JUN* (B/T cells) and *TIMP1* (all PBMCs except B cells and NKs). In contrast, in non-severe  
375 cases, it was *PTEN* (monocytes and platelets) and *ACAA1* (all PBMCs but especially B cells). Like  
376 *ACAA1*, which opposed its proteomic counterpart, *CKAP4* was also increased in non-severe cases  
377 (monocytes). Other active genes in all non-severe PBMCs were *FLT3LG*, *BAX*, *LYN* and *TNFSF10*,  
378 while *NCF2* was mainly in severe monocytes (Figure 5D-E) (Supplementary Material 5).

379 Overall, these results elaborate on the cellular origins of certain predictive drivers for severe COVID-  
380 19 inferred by APNet in PBMCs and were attained through APNet' noticeable versatility in bridging  
381 across -omic modalities.

382

383 **3.5 Benchmarking APNet against alternative ML/DL methods**

384 To benchmark APNet's significant performance on COVID-19 classification tasks, we initially  
385 retrieved from the literature the predictive models published by the authors of the MGH study (Filbin  
386 et al.), the Stanford study (Feyarts et al.), and of an independent study from Qatar which used the MGH  
387 study for independent validation. As shown in Table 1, APNet outperformed the MGH and Stanford  
388 models (Table 1). Although APNet showed similar performance to Qatar's predictive model (AUC >  
389 0.95, training-testing on the authors' in-house data) in demarcating severe COVID-19 cases, it  
390 outperformed Qatar's model in terms of generalizability. This was evident as the latter achieved an AUC  
391 of 0.79 when independently tested on the MGH study (Table 1).

392

393 **Table 1. Published ML/DL analyzing MGH and Stanford Olink datasets**

Study	AI model	AUC
Filbin et al. (MGH study)	Random Forest (elastic-net logistic regression with cross-validation)	0.85
Fayerts et al. (Stanford study)	(LASSO) linear regression	0.77 - 0.79 (Stanford study)
Al-Nesf et al. (Qatar study with Boruta algorithm)	MUVR	>0.959 (Qatar data) 0.76 (D0) (MGH validation)

394 At this point, we performed more specific benchmarking experiments using (a) a variation of APNet  
395 where we provided only DEPs to the DL model instead of DAPs (PASNet-expression) and (b) an  
396 alternative variation where we substituted the PASNet architecture with one of the most widely used,  
397 explainable Machine Learning approaches like Random Forest (RF). The training, validation and testing  
398 datasets remained the same as before.

399 Noticeably, APNet outperformed all alternative DL/ML models based on activity or expression data  
400 regarding AUC and F1-score (Figure 6A - B). More specifically, the PASNet-expression model  
401 performed poorly on the Mayo dataset (AUC: 0.645, F1 score: 0.7475), and none of the predicted  
402 molecules were hidden drivers. Biological explainability indicated ground-truth biological pathways  
403 related to COVID-19 immunopathology were the most predictive pathways. However, some more

404 nuanced pathways that APNet retrieved during the MGH-Mayo experiment were missing or under-  
405 represented (e.g., lipid imbalances) (Figure 6C-D).

406 The PASNet-expression model also under-performed in the Stanford study compared to APNet, with  
407 an AUC of 0.89 and an F1-score of 0.54. Unsurprisingly, this expression-driven investigation in the  
408 Stanford study could only reveal a limited scope of predictive biological pathways like Cellular  
409 response to stress, positive regulation of intracellular signaling transduction, Neutrophil degradation,  
410 and viral protein response (Figure 6E-F).

411 The second alternative model based on Random Forest (RF) under-performed even more on Mayo and  
412 Stanford datasets than the previous one since the models were validated with AUC: 0.65, F1-score:  
413 0.4746, and AUC: 0.7375, F1-score: 0.6486, respectively, for each dataset. Noticeably, the top-  
414 predictive proteins were almost identical across the Mayo and Stanford datasets analysis. Concerning  
415 the multi-omic experiment, we opted not to test the PASNet expression-driven model. This decision  
416 was based on the intrinsic sparsity of the scRNA-seq data's expression and the apparent requirement for  
417 specific data harmonization or more advanced ML/DL manipulations, which were beyond the scope of  
418 our current project. Consequently, we exclusively employed the RF model on the shared perturbational  
419 space identified through activity analysis between plasma proteomics and scRNA-seq data. This  
420 approach underperformed compared to APNet, as evidenced by an AUC of 0.87 and an F1-score of  
421 0.73 (Figure 6G).

422 With regards to associations with clinico-biological covariates, the most predictive proteins or drivers  
423 from the benchmarking studies exhibited correlations with COVID-19 severity but not to the extend  
424 that APNet's results did (e.g., this is evident in the expression-PASNet MGH-Mayo/Stanford and the  
425 RF MGH-Stanford experiments). Furthermore, associations with diabetes and kidney disease were not  
426 as straightforward as in the case of APNet (Supplementary Figure 6-7) (Supplementary Material 6).

427

### 428 **3.6 *In silico* evaluation of APNet's results based on COVID-19 curated prior knowledge**

429 To evaluate the degree of COVID-19 ground truths that APNet and the other classification models  
430 recovered, we mapped each model's top 20 most predictive proteins from the various experiments to  
431 the SIGNOR 3.0 COVID-19 Hallmark pathways (i.e. *Virus Entry*, *Cytokine storm*, *Inflammation*,  
432 *Fibrosis*, *Apoptosis*, *Innate response to dsRNA*, *MAPK Activation*, *ER stress and Stress granules*,  
433 <https://signor.uniroma2.it/covid/>). APNet's most predictive drivers from the MGH-Mayo and the multi-  
434 omic experiments were considerably over-represented (1.5 to 2 fold) on the SIGNOR 3.0 COVID-19  
435 Hallmark pathways than their counterparts from the PASNet-expression and RF models. Concerning  
436 the MGH-Stanford experiment, APNet and PASNet-expression exhibited almost an equal number of

437 mappings but different in type, while the RF model was again significantly under-represented. In the  
438 case of MAPK activation, a cardinal pathway in COVID-19 pathobiology, APNet accomplished  
439 approximately twice as many mappings (8) as the expression-PASNet model (4), revealing higher  
440 robustness in connecting predictive drivers of severity with COVID-19 biological underpinnings (Table  
441 2) (Supplementary material 7).

442 **Table 2. Biological benchmarking of APNet vs PASNet Expression and RF-Activity.** The table measures the number of  
443 top-20 predictive drivers that were mapped to the respective SIGNOR 3.0 pathway networks, in each classification experiment  
444 (SIGNOR 3.0 COVID-19 Hallmarks).

	MGH-Mayo			MGH-Stanford			scMGH	
SIGNOR 3.0 COVID-19 Hallmark	APNet	PASNet-Expression	RF-Activity	APNet	PASNet-Expression	RF-Activity	APNet	RF-Activity
<i>Virus Entry</i>	4	2	1	4	5	1	4	2
<i>Cytokine Storm</i>	5	5	0	5	7	0	7	3
<i>Inflammation</i>	6	5	0	9	7	0	7	2
<i>Fibrosis</i>	4	3	1	3	5	1	7	4
<i>Apoptosis</i>	9	5	1	8	7	1	5	2
<i>Innate response to dsRNA</i>	3	3	0	3	5	0	4	2
<i>MAPK activation</i>	6	3	1	8	5	1	6	3
<i>ER stress</i>	3	2	0	4	3	0	3	1
<i>Stress granules</i>	5	3	1	5	6	1	6	3
<i>Total mappings</i>	45	31	5	49	50	5	49	22

445

446

447 **3.7 APNet enables the creation of weighted graph models for mechanistic hypotheses: The case of  
448 ACAA1**

449 We postulated that combining SJARACNe co-expression networks, with pathways that APNet ingested  
450 as biological priors before classification tasks and the weights it assigned to them upon completion of  
451 demarcating severe COVID-19 could be helpful to *in silico* predict regulatory motifs and signaling  
452 patterns driving severe COVID-19.

453 To demonstrate this feature, we focused on the MGH-Mayo experiment, we assembled a multipartite  
454 graph of with driver-driver and driver-pathway connections and we sought to leverage information

455 about ACAA1 (Acetyl-CoA Acyltransferase 1), which was one of the top 20 most predictive drivers,  
456 was designated as a hidden driver by our analysis and it was significantly hypo-active in severe PBMCs  
457 which suggested the its plasma proteomic signature derived from an alternative tissue or organ.

458 By retrieving the MGH SJARACNe SHAP graph (a series of small positive, coherent feedforward loops  
459 with NCF2, TIMP1, CKAP4 as sources, TNFRSF10B as a significant “sink” and FLT3 as the primary  
460 inhibitor), it was apparent that no obvious connection existed between ACAA1 and the other predictive  
461 drivers (Figure 7A). To validate the biological plausibility of the SJARACNe graph, the respective PPI  
462 network from STRINGdb was leveraged (interaction score  $> 0.4$ ), indicating high interconnectivity for  
463 most of the predictive drivers. Interestingly, ACAA1 and CKAP4 remained unconnected  
464 (<https://version-12-0.string-db.org/cgi/network?networkId=bmlgZrzN1Cex>) (Figure 7B).

465 Next, considering that ACAA1 is predominantly expressed in the liver based on our previous GTEx  
466 analysis, we took inspiration from representation learning (Zitnik et al., 2019) and performed  
467 dimensionality reduction on the APNet complex graph with the tSNE algorithm, looking for maximum  
468 variance in liver expression based on TISSUES 2.0 scores. A distinct cluster with highly liver-specific  
469 drivers was detected. To gain a better insight on them, we isolated their subgraph with their most  
470 prognostic connected pathways (PASNet weight  $> 0.5$  and  $< -0.5$ ). We detected a graph “island” which  
471 contained four highly predictive drivers of COVID-19 severity among other proteins (ACAA1, SDC1,  
472 HGF, CKAP4) and connected pathways involved Immune System signaling, neutrophil degranulation,  
473 MAPK signaling, chaperone activation (HSP90) and VEGF signaling (Figure 7C-D).

474 Based on these findings, we posited that there should be an underlying connection between ACAA1  
475 and some of the other three predictive drivers of severity. We resorted to the OCSANA+ Cytoscape  
476 application to simulate signal propagation from SDC1, HGF and CKAP4 on the APNet complex graph.  
477 By calculating the Signal Flow Analysis (SFA, see Materials and Methods) metric, it became apparent  
478 that HGF and SDC1 signal propagation converged towards ACAA1 through various intermediate  
479 proteins. A similar effect on ACAA1 was not observed in the case of CKAP4, which did not appear to  
480 propagate any signal towards ACAA1 (Figure 7E).

481 To better elucidate these findings, we calculated the shortest paths from SDC1, HGF and CKAP4  
482 towards ACAA1 using the PathwayLinker application on Cytoscape. When selecting the “additive  
483 weight method” for the MI score as edge weight, PathLinker highlighted 2 critical shortest paths: (a) a  
484 signaling cascade commencing from SDC1 and reaching ACAA1 through KRT18 and GRPEL1 and  
485 (b) an incoherent feed-forward loop starting from HGF and through inhibiting ICOSLG which activated  
486 PTPRS which inhibited ACAA1. The “unweighted method” in PathwayLinker returned the same  
487 results. Notwithstanding, when selecting the “probabilistic weight method” for the MI score as edge

488 weight, PathwayLinker suggested a larger signaling cascade commencing from CKAP4, and extending  
489 through TRIAP1, LBR and GRPEL1 towards ACAA1 (Figure 7F).

490 To computationally validate these APNet shortest paths, we queried the STRINGdb database for the  
491 respective PPI networks. After 2 rounds of expansion, we retrieved a singular PPI network (14 nodes,  
492 23 edges, <https://version-12-0.string-db.org/cgi/network?networkId=b57tJ84II6T8>), connecting SDC1,  
493 GRPEL1, KRT18 and ACAA1 which upon k-means clustering revealed three components relative to  
494 fatty-acid metabolism (ACAA1, ACOX1, HADHA, HSD17B4, EHHADH), mitochondrial protein  
495 transport (HSPA9, KRT18, KRT8, GRPEL1, TIMM44) and cell surface interactions (FN1, SDC1,  
496 SDCBP, FGF2). In the case of the other shortest paths, the corresponding STRINGdb queries required  
497 more than 5 cycles of expansion to produce PPI networks encompassing all drivers of interest (CKAP4:  
498 55 nodes, 375 edges, <https://version-12-0.string-db.org/cgi/network?networkId=bjbqEWsYzPw4>;  
499 HGF: 44 nodes, 214 edges, <https://version-12-0.string-db.org/cgi/network?networkId=bcT9lsyOCwJ7>)  
500 (Sup. Figure 8).

501 Finally, as an additional step to assess the potential significance of these paths in a more COVID-19-  
502 specific biological context, we queried the BYCOVID19 data portal  
503 (<https://www.covid19dataportal.org/>) for the “COVID-19 association score” provided by the  
504 OpenTargets platform. SDC1 exhibited the highest score (0.555) with a considerable difference from  
505 some of the other drivers of severity (KRT18=0.05, LBR=0.004, CKAP4=0.006, HGF=0.025),  
506 confirming the biological prioritization of the SDC1-ACAA1 nascent connection that APNet uncovered  
507 (Supplementary Material 8-9).

508

509 **4. Discussion - Conclusion**

510 In the current work, focusing on COVID-19 omics, we present APNet, a computational DL pipeline to  
511 elucidate complex biological motifs while classifying patients based on their clinical severity.

512 APNet is inspired by computational approaches modeling Gene Regulatory Networks (GRNs), which  
513 have been instrumental in discovering new interactions between biological entities and formulating  
514 novel scientific hypotheses. APNet combines some of the best practices in the field by combining an  
515 Information Theory model (SJARACNe algorithm) through a Bayesian scope (NetBID2/scMINER  
516 toolkits) (Delgado and Gómez-Vela, 2019) and a biologically-informed neural network with enhanced  
517 explainability (PASNet and SHAP values) for supervised patient clustering. The above bioinformatic  
518 tools have been shown independently to effectively discover potential biomarkers and druggable targets  
519 in diseases however, to the best of our knowledge, they have never been used as a unified pipeline for  
520 COVID-19 or any other disease type (Wang et al., 2021) (Ding et al., 2023) (Hao et al., 2018).

521 In our study, we utilized APNet to predict severe COVID-19 cases in three different Olink plasma  
522 proteomic datasets (MGH, Mayo, Stanford), and a complementary scRNA-seq study. APNet conducted  
523 biologically informed predictions using driver-pathway associations (KEGG, Reactome, GO:BP,  
524 Wikipathways) with remarkable robustness, outperforming alternative ML/DL approaches which either  
525 lacked (a) the activity transformations enabled by the NetBID2/scMINER toolkits (PASNet-expression  
526 model) or (b) the PASNet DL architecture (Random Forest classifications). Based on the biological  
527 explainability of each model (SHAP values, driver-pathway mapping with learning DL weights) and  
528 COVID-19 curated biological ground-truths (SINGOR COVID-19 pathway networks), evidently,  
529 APNet was able to better approximate the systemic nature of severe COVID-19 from the provided  
530 biological data. We posit that APNet performed so efficiently due to the sparse regularization of the  
531 hierarchical relationships of drivers and pathways after initial differential activity analysis. Hence,  
532 APNet was able to capture both well known but also more nuanced perturbations in severe COVID-19  
533 (i.e., known drivers but also “hidden drivers” like ACAA1, FLT3) implicating several potential tissues  
534 of origin and a diverse repertoire of critical pathways. Indicatively, some of the most predictive drivers  
535 and pathways that APNet captured concerned apoptosis, dishevelled PI3K-Akt stimulation  
536 (FLT3/FLT3LG, PTEN, NTF4, KIT), neurodegeneration (EGFR, SEMAD4), cell differentiation  
537 (TNFSF11), neutrophil degranulation (ACAA1), lipid metabolism (TNFRSF10A), immune and  
538 interleukin signaling (CD63, TIMP1, JUN), T cell receptor signaling (BIRC2, NFATC1, CD4,  
539 IKBKG), oxidative phosphorylation (ATP6AP2). These signaling cascades and some of these drivers  
540 have already been implicated with COVID-19, which attests to APNet’s overall capacity to make  
541 biologically plausible predictions. (Basile et al., 2022; Chidambaram et al., 2022; Merad and Martin,  
542 2020; Pistollato et al., 2022; Thompson et al., 2021). A paradigmatic case concerning the translational  
543 value of APNet’s findings was the implication of MAPK pathway in severe COVID-19 based on various  
544 drivers (e.g., MAPK9, AREG, KIT, JUN, FLT3LG). These drivers were not prioritized to the same  
545 extend as highly predictive by the alternative ML/DL models – if prioritized at all. This could explain  
546 in part why APNet surpassed these models as a classifier of COVID-19 severity since components of  
547 the MAPK pathway (sH-RAS, C-RAF, MAPK1, MAPK2 and ERK) have emerged as critical tenets of  
548 Sars-CoV-2 tropism in PBMCs and have been associated with adverse clinical covariates like hypoxia,  
549 dyspnoea and vascular damages (Cusato et al., 2023).

550 Finally, APNet extends beyond biological explainability to actionability regarding the formulation of  
551 mechanistic hypotheses, by providing the capacity to generate a weighted driver-pathway network that  
552 incorporates information from SJARACNe co-expression networks, the differential activity analysis,  
553 the PASNet DL clinical predictions and external dedicated bioinformatic databases like STRINGdb.  
554 APNet enabled through graph representation learning, shortest path detection, and signal propagation  
555 simulation the prediction of a liver-specific signaling cascade in severe COVID-19 involving ACAA1  
556 (*hidden driver with prognostic significance but no apparent connections to other predictive drivers*),

557 SDC1, KRT18, and GRPEL1. These predictions are not biologically implausible given the implication  
558 of SDC1 and KRT18 in inflammation and epithelial damage (Ghondaghsaz et al., 2023; Liao et al.,  
559 2020), the involvement of the mitochondrial GRPEL1 in host/Sars-CoV-2 interactions (Zhang et al.,  
560 2022), the clinical correlation of ACAA1 (a mediator of fatty acid oxidation in the mitochondria and  
561 the peroxisomes) with ICU-admittance in COVID-19 (Penrice-Randal et al., 2022) and a severe  
562 mitochondria dysfunction in the liver of severe COVID-19 cases (Guarnieri et al., 2023).

563 The work herein is not without its limitations. One limitation concerns the restricted number of studies  
564 involved and the binary assignment of drivers to pathways. Pathway activation is a dynamic process  
565 controlled by fluctuations in expression or activity changes of a protein or drivers, respectively. Outputs  
566 from more advanced pathway enrichment techniques like GSEA could be more instructive for the DL  
567 model to perform classifications more aptly. Another limitation is the need to perform several manual  
568 steps in APNet's complex graphs to test hypotheses and leverage new insights, which might hinder data  
569 exploration and analysis. Another issue worth noting is that APNet does not include clinical covariates  
570 as clinical-biological priors, which could be addressed in the future by adopting in our pipeline the more  
571 clinically-oriented version of Cox-PASNet (Hao et al., 2019).

572 Overall, APNet is a robust pipeline that can simplify the extraction of intricate biological insights from  
573 complex biological data while also performing clinical predictions and testing mechanistic hypotheses.  
574 *In vitro/in vivo* validations should accompany future implementations of APNet to validate the  
575 pipeline's true translational credibility. Additionally, APNet's scalability to other multi-factorial  
576 disease-omic datasets (such as cancer and neurodegenerative diseases) should be explored along with  
577 its potential deployment in other computational tasks (like multi-omic data integration and interactions  
578 with knowledge graph pipelines).

579  
580  
581  
582  
583  
584  
585  
586  
587  
588  
589  
590  
591

592

593 **Disclosures**

594 None.

595

596 **Funding**

597 This work was funded by the HORIZON-INFRA-2021-EOSC-01-04 project **Scilake**  
598 (<https://scilake.eu/>). Also, this work was also supported by ELIXIR (<https://elixir-europe.org/>), the  
599 research infrastructure for life-science data.

600

601 **Competing interests**

602 None.

603

604 **Author Contributions**

605 Conceptualization, resources, methodology, investigation, formal analysis, writing – original draft,  
606 writing – review & editing: G.I.G, V.I.V., S.D. Supplementary analysis by G.K. Supervision: A.G.,  
607 G.A.P., F.P.

608

609 **Data Availability**

610 APNet R and Python scripts and the code to re-create the figures of this manuscript can be found at  
611 <https://github.com/BiodataAnalysisGroup/APNet>.

612 The datasets used in this study can be accessed in the following links: **MGH Olink proteomics**:  
613 <https://info.olink.com/mgh-covid-study-overview-page?hsCtaTracking=fff99a2a-81c1-4e4a-a70d-6922d26503b4%7C202c2809-0976-48f7-aad0-3903c36624ca>, **Mayo Olink Proteomics**:  
614 [https://www.thelancet.com/journals/landig/article/PIIS2589-7500\(22\)00112-1/fulltext#supplementaryMaterial](https://www.thelancet.com/journals/landig/article/PIIS2589-7500(22)00112-1/fulltext#supplementaryMaterial), **Stanford Olink proteomics**:  
615 <https://datadryad.org/stash/dataset/doi:10.5061/dryad.9cnp5hqm>, **single-cell MGH Villani group**:  
616 <https://www.covid19cellatlas.org/index.patient.html> . All of the above data are also included in our  
617 Zenodo link: 10.5281/zenodo.10438830

620 Other supplementary material can be found at the “Supplementary Materials for Online” folder and on  
621 Zenodo: 10.5281/zenodo.10438830

622

623 **Description of supplementary materials**

624

625

File name	Description
Supplementary_Material_1_DOME.pdf	DOME recommendations for the APNet models
Supplementary_Material_2_MGH_Mayo_Stanford_matrices.xlsx	Expression, and Activity matrices for MGH, Mayo, and Stanford datasets
Supplementary_Material_3_DA_MGH_Mayo_Stanford.xlsx	Differential Activity outputs of MGH, Mayo, Stanford and their relevant master file
Supplementary_Material_4_APNet_weights.xlsx	APNet activity s1_weights outputs for MGH-Mayo, MGH-Stanford
Supplementary_Material_5_scMGH_MGH.xlsx	Differential Activity outputs of scMGH + APNet activity s1_weights outputs for MGH-scMGH
Supplementary_Material_6_PASNet_Expr_Benchmarking.xlsx	PASNet expression s1_weights outputs for MGH-Mayo, MGH-Stanford
Supplementary_Material_7_SIGNOR_COVID_Hallmarks.cys	Cytoscape file that contains the SIGNOR 3.0 COVID-19 hallmark pathways and the mapping of the most predictive drivers from APNet and the benchmarking experiments
Supplementary_Material_8_The_ACAA1_case_study.cys	Cytoscape file that contains the bipartite driver-pathway weighted network based on the MGH SJARACNe co-expression graph (MGH-Mayo experiment). This bipartite network is used to leverage information about ACAA1.
Supplementary_Material_9_The_ACAA1_case_study_OCSANA.txt	Txt file guiding through the Cytoscape analysis for the ACAA1 case study.

626

627

628

629

630

631

632

633

634

## 5. Bibliography

635 Babačić, H., Christ, W., Araújo, J.E., Mermelekas, G., Sharma, N., Tynell, J., García, M., Varnaite,  
636 R., Asgeirsson, H., Glans, H., Lehtiö, J., Gredmark-Russ, S., Klingström, J., Pernemalm, M.,  
637 2023. Comprehensive proteomics and meta-analysis of COVID-19 host response. *Nat.*  
638 *Commun.* 14, 5921. <https://doi.org/10.1038/s41467-023-41159-z>

639 Basile, M.S., Cavalli, E., McCubrey, J., Hernández-Bello, J., Muñoz-Valle, J.F., Fagone, P., Nicoletti,  
640 F., 2022. The PI3K/Akt/mTOR pathway: A potential pharmacological target in COVID-19.  
641 *Drug Discov. Today* 27, 848–856. <https://doi.org/10.1016/j.drudis.2021.11.002>

642 Byeon, S.K., Madugundu, A.K., Garapati, K., Ramarajan, M.G., Saraswat, M., Kumar-M, P., Hughes,  
643 T., Shah, R., Patnaik, M.M., Chia, N., Ashrafzadeh-Kian, S., Yao, J.D., Pritt, B.S., Cattaneo,  
644 R., Salama, M.E., Zenka, R.M., Kipp, B.R., Grebe, S.K.G., Singh, R.J., Sadighi Akha, A.A.,  
645 Algeciras-Schimminich, A., Dasari, S., Olson, J.E., Walsh, J.R., Venkatakrishnan, A.J.,  
646 Jenkinson, G., O’Horo, J.C., Badley, A.D., Pandey, A., 2022. Development of a multiomics  
647 model for identification of predictive biomarkers for COVID-19 severity: a retrospective  
648 cohort study. *Lancet Digit. Health* 4, e632–e645. [https://doi.org/10.1016/S2589-7500\(22\)00112-1](https://doi.org/10.1016/S2589-7500(22)00112-1)

649 Chidambaram, V., Kumar, A., Majella, M.G., Seth, B., Sivakumar, R.K., Voruganti, D., Bavineni, M.,  
650 Baghal, A., Gates, K., Kumari, A., Al’Aref, S.J., Galiatsatos, P., Karakousis, P.C., Mehta,  
651 J.L., 2022. HDL cholesterol levels and susceptibility to COVID-19. *eBioMedicine* 82,  
652 104166. <https://doi.org/10.1016/j.ebiom.2022.104166>

653 Cusato, J., Manca, A., Palermi, A., Mula, J., Costanzo, M., Antonucci, M., Trunfio, M., Corcione,  
654 S., Chiara, F., De Vivo, E.D., Ianniello, A., Ferrara, M., Di Perri, G., De Rosa, F.G.,  
655 D’Avolio, A., Calcagno, A., 2023. COVID-19: A Possible Contribution of the MAPK  
656 Pathway. *Biomedicines* 11, 1459. <https://doi.org/10.3390/biomedicines11051459>

657 Delgado, F.M., Gómez-Vela, F., 2019. Computational methods for Gene Regulatory Networks  
658 reconstruction and analysis: A review. *Artif. Intell. Med.* 95, 133–145.  
659 <https://doi.org/10.1016/j.artmed.2018.10.006>

660 Diamond, M.S., Kanneganti, T.-D., 2022. Innate immunity: the first line of defense against SARS-  
661 CoV-2. *Nat. Immunol.* 23, 165–176. <https://doi.org/10.1038/s41590-021-01091-0>

662 Dimitraki, S., Gavriilidis, G.I., Dimitriadis, V.K., Natsiavas, P., 2023. Benchmarking of Machine  
663 Learning classifiers on plasma proteomic for COVID-19 severity prediction through  
664 interpretable artificial intelligence. *Artif. Intell. Med.* 137, 102490.  
665 <https://doi.org/10.1016/j.artmed.2023.102490>

666 Ding, L., Shi, H., Qian, C., Burdyshaw, C., Veloso, J.P., Khatamian, A., Pan, Q., Dhungana, Y., Xie,  
667 Z., Risch, I., Yang, X., Huang, X., Yan, L., Rusch, M., Brewer, M., Yan, K.-K., Chi, H., Yu,  
668 J., 2023. scMINER: a mutual information-based framework for identifying hidden drivers  
669 from single-cell omics data. *BioRxiv Prepr. Serv. Biol.*  
670 <https://doi.org/10.1101/2023.01.26.523391>

671 Ding, L., Shi, H., Qian, C., Burdyshaw, C., Veloso, J.P., Pan, Q., Dhungana, Y., Xie, Z., Risch, I.,  
672 Yang, X., Yan, L., Rusch, M., Brewer, M., Yan, K.-K., Chi, H., n.d. scMINER: a mutual  
673 information-based framework for identifying hidden drivers from single-cell omics data.

674 Dong, X., Ding, L., Thrasher, A., Wang, X., Liu, J., Pan, Q., Rash, J., Dhungana, Y., Yang, X., Risch,  
675 I., Li, Y., Yan, L., Rusch, M., McLeod, C., Yan, K.-K., Peng, J., Chi, H., Zhang, J., Yu, J.,  
676 2023. NetBID2 provides comprehensive hidden driver analysis. *Nat. Commun.* 14, 2581.  
677 <https://doi.org/10.1038/s41467-023-38335-6>

678 Eldjarn, G.H., Ferkingstad, E., Lund, S.H., Helgason, H., Magnusson, O.Th., Gunnarsdottir, K.,  
679 Olafsdottir, T.A., Halldorsson, B.V., Olason, P.I., Zink, F., Gudjonsson, S.A.,  
680 Sveinbjornsson, G., Magnusson, M.I., Helgason, A., Oddsson, A., Halldorsson, G.H.,  
681 Magnusson, M.K., Saevarsdottir, S., Eiriksdottir, T., Masson, G., Stefansson, H., Jonsdottir,  
682 I., Holm, H., Rafnar, T., Melsted, P., Saemundsdottir, J., Nordahl, G.L., Thorleifsson, G.,  
683 Ulfarsson, M.O., Gudbjartsson, D.F., Thorsteinsdottir, U., Sulem, P., Stefansson, K., 2023.  
684 Large-scale plasma proteomics comparisons through genetics and disease associations. *Nature*  
685 622, 348–358. <https://doi.org/10.1038/s41586-023-06563-x>

686

687 Evangelista, J.E., Xie, Z., Marino, G.B., Nguyen, N., Clarke, D.J.B., Ma'ayan, A., 2023. Enrichr-KG:  
688 bridging enrichment analysis across multiple libraries. *Nucleic Acids Res.* 51, W168–W179.  
689 <https://doi.org/10.1093/nar/gkad393>

690 Feyaerts, D., Hédou, J., Gillard, J., Chen, H., Tsai, E.S., Peterson, L.S., Ando, K., Manohar, M., Do,  
691 E., Dhondalay, G.K.R., Fitzpatrick, J., Artandi, M., Chang, I., Snow, T.T., Chinthrajah, R.S.,  
692 Warren, C.M., Wittman, R., Meyerowitz, J.G., Ganio, E.A., Stelzer, I.A., Han, X., Verdonk,  
693 F., Gaudillière, D.K., Mukherjee, N., Tsai, A.S., Rumer, K.K., Jacobsen, D.R., Bjornson-  
694 Hooper, Z.B., Jiang, S., Saavedra, S.F., Valdés Ferrer, S.I., Kelly, J.D., Furman, D.,  
695 Aghaeepour, N., Angst, M.S., Boyd, S.D., Pinsky, B.A., Nolan, G.P., Nadeau, K.C.,  
696 Gaudillière, B., McIlwain, D.R., 2022. Integrated plasma proteomic and single-cell immune  
697 signaling network signatures demarcate mild, moderate, and severe COVID-19. *Cell Rep.*  
698 *Med.* 3, 100680. <https://doi.org/10.1016/j.xcrm.2022.100680>

699 Filbin, M.R., Mehta, A., Schneider, A.M., Kays, K.R., Guess, J.R., Gentili, M., Fenyves, B.G.,  
700 Charland, N.C., Gonye, A.L.K., Gushterova, I., Khanna, H.K., LaSalle, T.J., Lavin-Parsons,  
701 K.M., Lilley, B.M., Lodenstein, C.L., Manakongtreeeep, K., Margolin, J.D., McKaig, B.N.,  
702 Rojas-Lopez, M., Russo, B.C., Sharma, N., Tantivit, J., Thomas, M.F., Gerszten, R.E.,  
703 Heimberg, G.S., Hoover, P.J., Lieb, D.J., Lin, B., Ngo, D., Pelka, K., Reyes, M., Smillie,  
704 C.S., Waghray, A., Wood, T.E., Zajac, A.S., Jennings, L.L., Grundberg, I., Bhattacharyya,  
705 Parry, B.A., Villani, A.-C., Sade-Feldman, M., Hacohen, N., Goldberg, M.B., 2021.  
706 Longitudinal proteomic analysis of severe COVID-19 reveals survival-associated signatures,  
707 tissue-specific cell death, and cell-cell interactions. *Cell Rep. Med.* 2, 100287.  
708 <https://doi.org/10.1016/j.xcrm.2021.100287>

709 Ghondaghsaz, E., Khalaji, A., Norouzi, M., Fraser, D.D., Alilou, S., Behnoush, A.H., 2023. The  
710 utility of syndecan-1 circulating levels as a biomarker in patients with previous or active  
711 COVID-19: a systematic review and meta-analysis. *BMC Infect. Dis.* 23, 510.  
712 <https://doi.org/10.1186/s12879-023-08473-9>

713 Gil, D.P., Law, J.N., Murali, T.M., 2017. The PathLinker app: Connect the dots in protein interaction  
714 networks. *F1000Research* 6, 58. <https://doi.org/10.12688/f1000research.9909.1>

715 Guarnieri, J.W., Dybas, J.M., Fazelinia, H., Kim, M.S., Frere, J., Zhang, Y., Soto Albrecht, Y.,  
716 Murdock, D.G., Angelin, A., Singh, L.N., Weiss, S.L., Best, S.M., Lott, M.T., Zhang, S.,  
717 Cope, H., Zaksas, V., Saravia-Butler, A., Meydan, C., Foox, J., Mozsary, C., Bram, Y.,  
718 Kidane, Y., Priebe, W., Emmett, M.R., Meller, R., Demharter, S., Stentoft-Hansen, V.,  
719 Salvatore, M., Galeano, D., Enguita, F.J., Grabham, P., Trovao, N.S., Singh, U., Haltom, J.,  
720 Heise, M.T., Moorman, N.J., Baxter, V.K., Madden, E.A., Taft-Benz, S.A., Anderson, E.J.,  
721 Sanders, W.A., Dickmander, R.J., Baylin, S.B., Wurtele, E.S., Moraes-Vieira, P.M., Taylor,  
722 D., Mason, C.E., Schisler, J.C., Schwartz, R.E., Beheshti, A., Wallace, D.C., 2023. Core  
723 mitochondrial genes are down-regulated during SARS-CoV-2 infection of rodent and human  
724 hosts. *Sci. Transl. Med.* 15, eabq1533. <https://doi.org/10.1126/scitranslmed.abq1533>

725 Hao, J., Kim, Y., Kim, T.-K., Kang, M., 2018. PASNet: pathway-associated sparse deep neural  
726 network for prognosis prediction from high-throughput data. *BMC Bioinformatics* 19, 510.  
727 <https://doi.org/10.1186/s12859-018-2500-z>

728 Hao, J., Kim, Y., Mallavarapu, T., Oh, J.H., Kang, M., 2019. Interpretable deep neural network for  
729 cancer survival analysis by integrating genomic and clinical data. *BMC Med. Genomics* 12,  
730 189. <https://doi.org/10.1186/s12920-019-0624-2>

731 Liang, X., Sun, R., Wang, J., Zhou, K., Li, J., Chen, S., Lyu, M., Li, S., Xue, Z., Shi, Y., Xie, Y.,  
732 Zhang, Q., Yi, X., Pan, J., Wang, D., Xu, J., Zhu, H., Zhu, G., Zhu, J., Zhu, Y., Zheng, Y.,  
733 Shen, B., Guo, T., 2023. Proteomics Investigation of Diverse Serological Patterns in COVID-  
734 19. *Mol. Cell. Proteomics* 22, 100493. <https://doi.org/10.1016/j.mcpro.2023.100493>

735 Liao, M., Liu, Y., Yuan, J., Wen, Y., Xu, G., Zhao, J., Cheng, L., Li, J., Wang, X., Wang, F., Liu, L.,  
736 Amit, I., Zhang, S., Zhang, Z., 2020. Single-cell landscape of bronchoalveolar immune cells  
737 in patients with COVID-19. *Nat. Med.* 26, 842–844. <https://doi.org/10.1038/s41591-020-0901-9>

738 Marazzi, L., Gainer-Dewar, A., Vera-Licona, P., 2020. OCSANA+: optimal control and simulation of  
739 signaling networks from network analysis. *Bioinformatics* 36, 4960–4962.  
740 <https://doi.org/10.1093/bioinformatics/btaa625>

742 Merad, M., Martin, J.C., 2020. Pathological inflammation in patients with COVID-19: a key role for  
743 monocytes and macrophages. *Nat. Rev. Immunol.* 20, 355–362.  
744 <https://doi.org/10.1038/s41577-020-0331-4>

745 Paul, S.G., Saha, A., Biswas, A.A., Zulfiker, Md.S., Arefin, M.S., Rahman, Md.M., Reza, A.W.,  
746 2023. Combating Covid-19 using machine learning and deep learning: Applications,  
747 challenges, and future perspectives. *Array* 17, 100271.  
748 <https://doi.org/10.1016/j.array.2022.100271>

749 Penrice-Randal, R., Dong, X., Shapanis, A.G., Gardner, A., Harding, N., Legebeke, J., Lord, J.,  
750 Vallejo, A.F., Poole, S., Brendish, N.J., Hartley, C., Williams, A.P., Wheway, G., Polak,  
751 M.E., Strazzeri, F., Schofield, J.P.R., Skipp, P.J., Hiscox, J.A., Clark, T.W., Baralle, D., 2022.  
752 Blood gene expression predicts intensive care unit admission in hospitalised patients with  
753 COVID-19. *Front. Immunol.* 13, 988685. <https://doi.org/10.3389/fimmu.2022.988685>

754 Pistollato, F., Petrillo, M., Clerbaux, L.-A., Leoni, G., Ponti, J., Bogni, A., Brogna, C., Cristoni, S.,  
755 Sanges, R., Mendoza-de Gyves, E., Fabbri, M., Querci, M., Soares, H., Munoz, A., Whelan,  
756 M., Van de Eede, G., 2022. Effects of spike protein and toxin-like peptides found in COVID-  
757 19 patients on human 3D neuronal/glial model undergoing differentiation: Possible  
758 implications for SARS-CoV-2 impact on brain development. *Reprod. Toxicol.* 111, 34–48.  
759 <https://doi.org/10.1016/j.reprotox.2022.04.011>

760 Thompson, E.A., Cascino, K., Ordonez, A.A., Zhou, W., Vaghasia, A., Hamacher-Brady, A., Brady,  
761 N.R., Sun, I.-H., Wang, R., Rosenberg, A.Z., Delannoy, M., Rothman, R., Fenstermacher, K.,  
762 Sauer, L., Shaw-Saliba, K., Bloch, E.M., Redd, A.D., Tobian, A.A.R., Horton, M., Smith, K.,  
763 Pekosz, A., D'Alessio, F.R., Yegnasubramanian, S., Ji, H., Cox, A.L., Powell, J.D., 2021.  
764 Metabolic programs define dysfunctional immune responses in severe COVID-19 patients.  
765 *Cell Rep.* 34, 108863. <https://doi.org/10.1016/j.celrep.2021.108863>

766 Walsh, I., Fishman, D., Garcia-Gasulla, D., Titma, T., Pollastri, G., ELIXIR Machine Learning Focus  
767 Group, Capriotti, E., Casadio, R., Capella-Gutierrez, S., Cirillo, D., Del Conte, A.,  
768 Dimopoulos, A.C., Del Angel, V.D., Dopazo, J., Fariselli, P., Fernández, J.M., Huber, F.,  
769 Kreshuk, A., Lenaerts, T., Martelli, P.L., Navarro, A., Broin, P.Ó., Piñero, J., Piovesan, D.,  
770 Reczko, M., Ronzano, F., Satagopam, V., Savojardo, C., Spiwok, V., Tangaro, M.A., Tartari,  
771 G., Salgado, D., Valencia, A., Zambelli, F., Harrow, J., Psomopoulos, F.E., Tosatto, S.C.E.,  
772 2021. DOME: recommendations for supervised machine learning validation in biology. *Nat.*  
773 *Methods* 18, 1122–1127. <https://doi.org/10.1038/s41592-021-01205-4>

774 Wang, F., Morita, K., DiNardo, C.D., Furudate, K., Tanaka, T., Yan, Y., Patel, K.P., MacBeth, K.J.,  
775 Wu, B., Liu, G., Frattini, M., Matthews, J.A., Little, L.D., Gumb, C., Song, X., Zhang, J.,  
776 Thompson, E.J., Kadia, T.M., Garcia-Manero, G., Jabbour, E., Ravandi, F., Bhalla, K.N.,  
777 Konopleva, M., Kantarjian, H.M., Andrew Futreal, P., Takahashi, K., 2021. Leukemia  
778 stemness and co-occurring mutations drive resistance to IDH inhibitors in acute myeloid  
779 leukemia. *Nat. Commun.* 12, 2607. <https://doi.org/10.1038/s41467-021-22874-x>

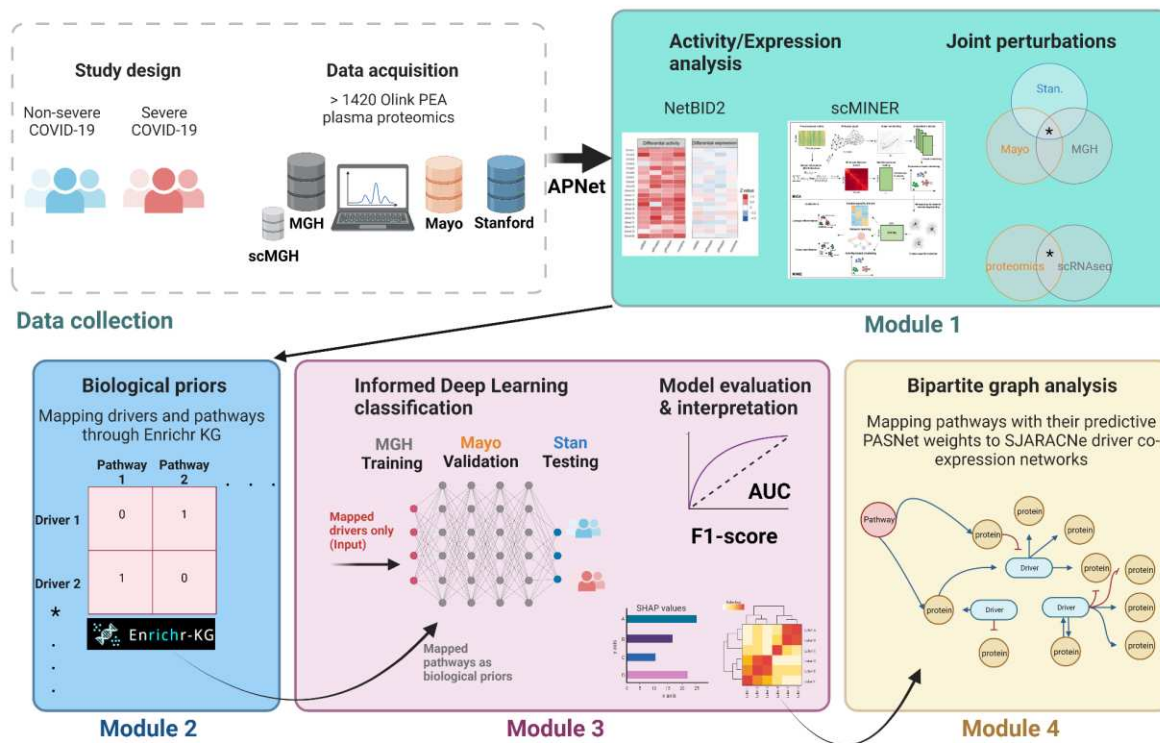
780 Wik, L., Nordberg, N., Broberg, J., Björkesten, J., Assarsson, E., Henriksson, S., Grundberg, I.,  
781 Pettersson, E., Westerberg, C., Liljeroth, E., Falck, A., Lundberg, M., 2021. Proximity  
782 Extension Assay in Combination with Next-Generation Sequencing for High-throughput  
783 Proteome-wide Analysis. *Mol. Cell. Proteomics* 20, 100168.  
784 <https://doi.org/10.1016/j.mcpro.2021.100168>

785 Zhang, N., Wang, S., Wong, C.C.L., 2022. Proteomics research of SARS-CoV-2 and COVID-19  
786 disease. *Med. Rev.* 2, 427–445. <https://doi.org/10.1515/mr-2022-0016>

787 Zhong, W., Edfors, F., Gummesson, A., Bergström, G., Fagerberg, L., Uhlén, M., 2021. Next  
788 generation plasma proteome profiling to monitor health and disease. *Nat. Commun.* 12, 2493.  
789 <https://doi.org/10.1038/s41467-021-22767-z>

790 Zitnik, M., Nguyen, F., Wang, B., Leskovec, J., Goldenberg, A., Hoffman, M.M., 2019. Machine  
791 learning for integrating data in biology and medicine: Principles, practice, and opportunities.  
792 *Inf. Fusion* 50, 71–91. <https://doi.org/10.1016/j.inffus.2018.09.012>

793

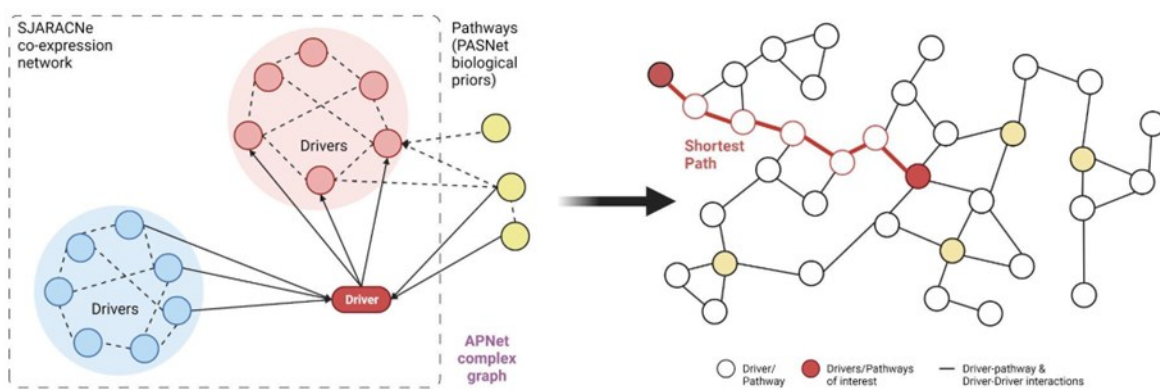


794

795 **Figure 1.** APNet workflow, as implemented in the herein COVID-19 multi-omic study to discover predictive drivers of  
796 severity. Image made using the Biorender toolkit.

797

798



799

800 **Figure 2.** Outline of APNet complex graph and the ensuing analysis with shortest path algorithms for uncovering non-intuitive  
801 connections among drivers and pathways.

802

803

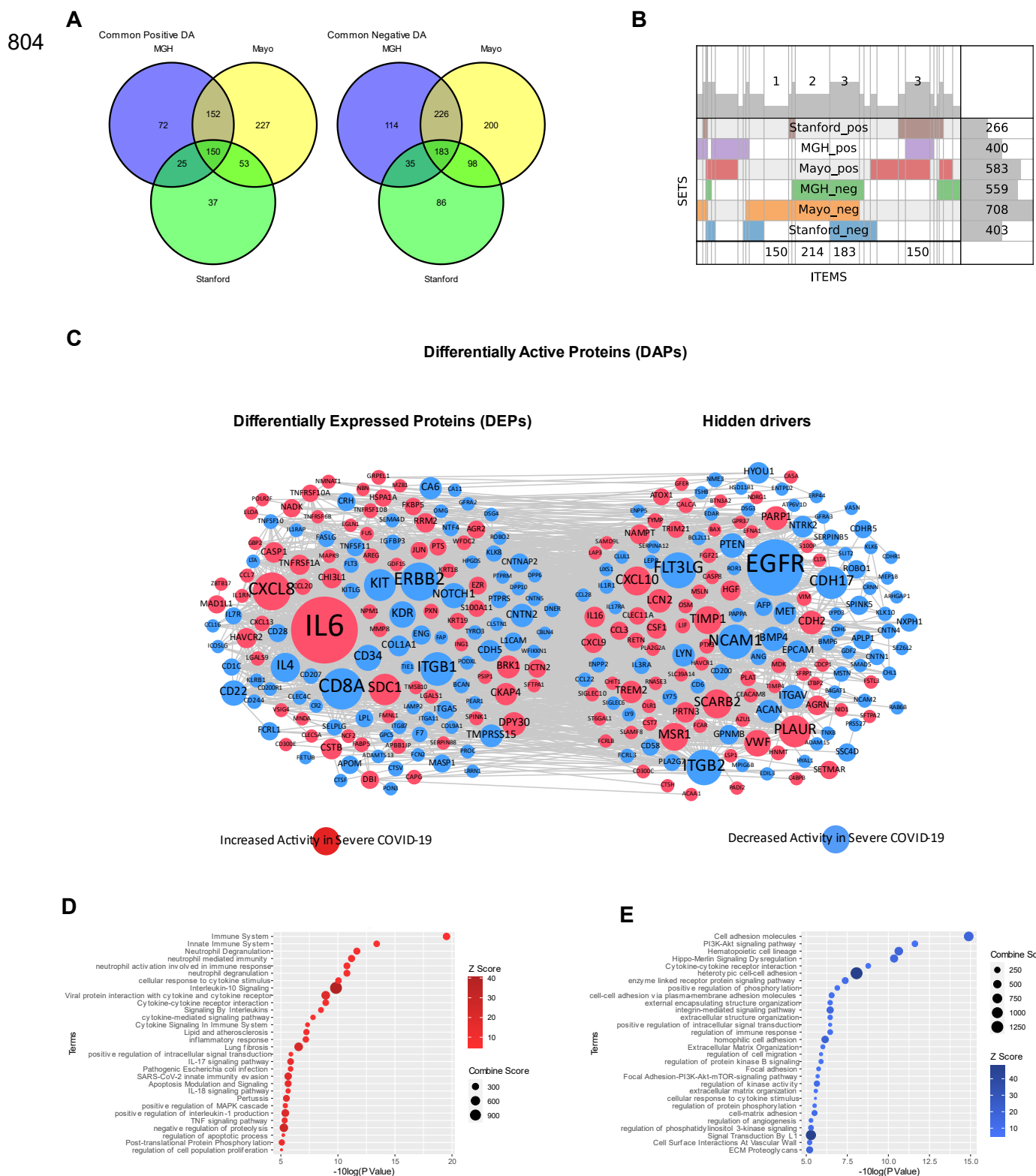
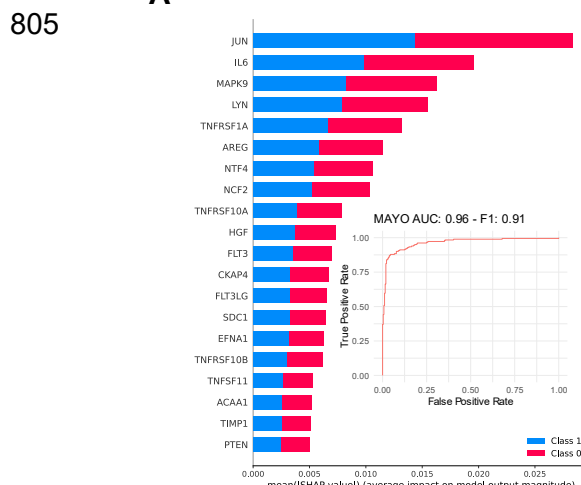


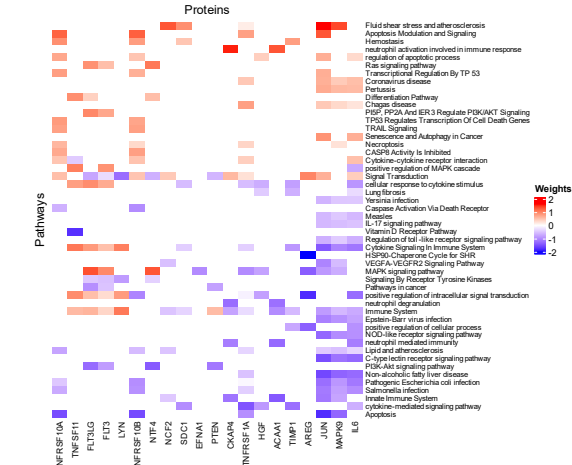
**Figure 3. APNet uncovers a large COVID-19 perturbational proteomic space underpinning the 3 distinct Olink datasets (MGH, Mayo, Stanford).** (A) Venn diagrams showing overlapping differentially expressed proteins (DEPs) and differentially active proteins (DAGs) among the three studies. (B) SuperVenn diagram depicting the joint differentially expressed (increased/decreased) or active proteins (hyper/hypo-active) in severe COVID-19 compared to non-severe COVID-19 cases, across the three Olink studies. (C) STRINGdb protein-protein interaction networks for joint DEPs and hidden drivers of severity across the three studies (STRINGdb score > 0.4). The size of the nodes is analogous to the centrality of each protein/driver (BetweennessCentrality algorithm) and the colour denotes perturbational direction (red for increased, blue for decreased). (D-E) Bubble plots depicting over-representation analysis based on the Enrichr Knowledge Graph (Wikipathways 2021, Reactome, GO:BP, KEGG) for joint drivers with increased (D) and decreased activity (E) in severe COVID-19 cases, among the three Olink plasma proteomic studies.

APNet uncovers predictive drivers of COVID-19 severity

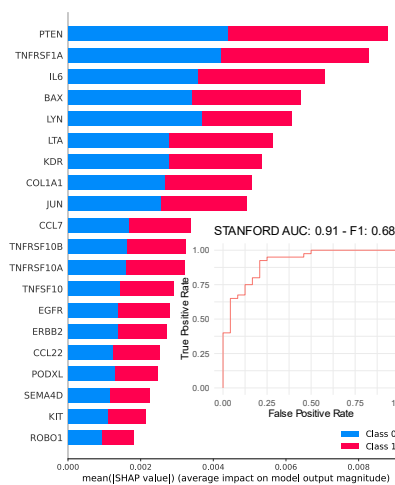
**A**



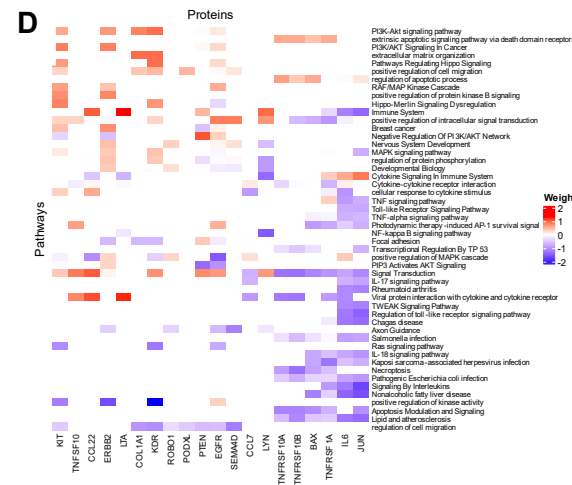
**B**



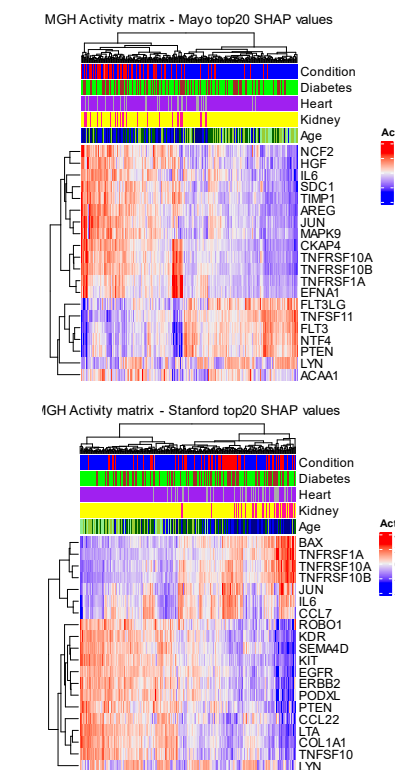
**C**



**D**



**E**



Mayo Activity - Mayo top20 SHAP values

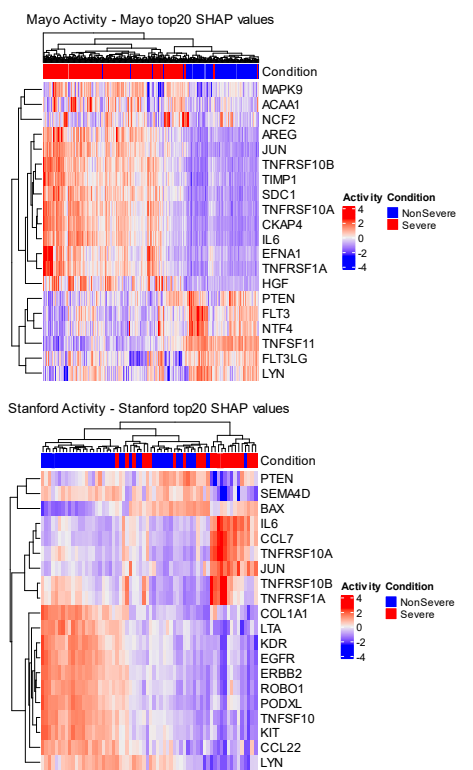


**Figure 4. APNet deploys sparse regularization of driver-pathway connections through the PASNet Deep Learning model and robustly classifies severe from non-severe COVID-19 cases in the three Olink proteomic studies. (A-B)** Bar plots for SHAP values and driver-pathway mapping from PASNet signifying the top-20 predictive drivers and their corresponding pathways, for the MGH (training) / Mayo (testing) experiment. Furthermore, the AUC and F1-score values are depicted. **(C-D)** Same as (A) for the MGH (training) / Stanford (testing) experiment. Class 0 refers to nonsevere and Class 1 refers to severe COVID-19 cases. **(E)** Hierarchical clustering of MGH, Mayo and Stanford cases on the basis on the predictive proteomic drivers, along with selected clinical covariates.

APNet uncovers predictive drivers of COVID-19 severity

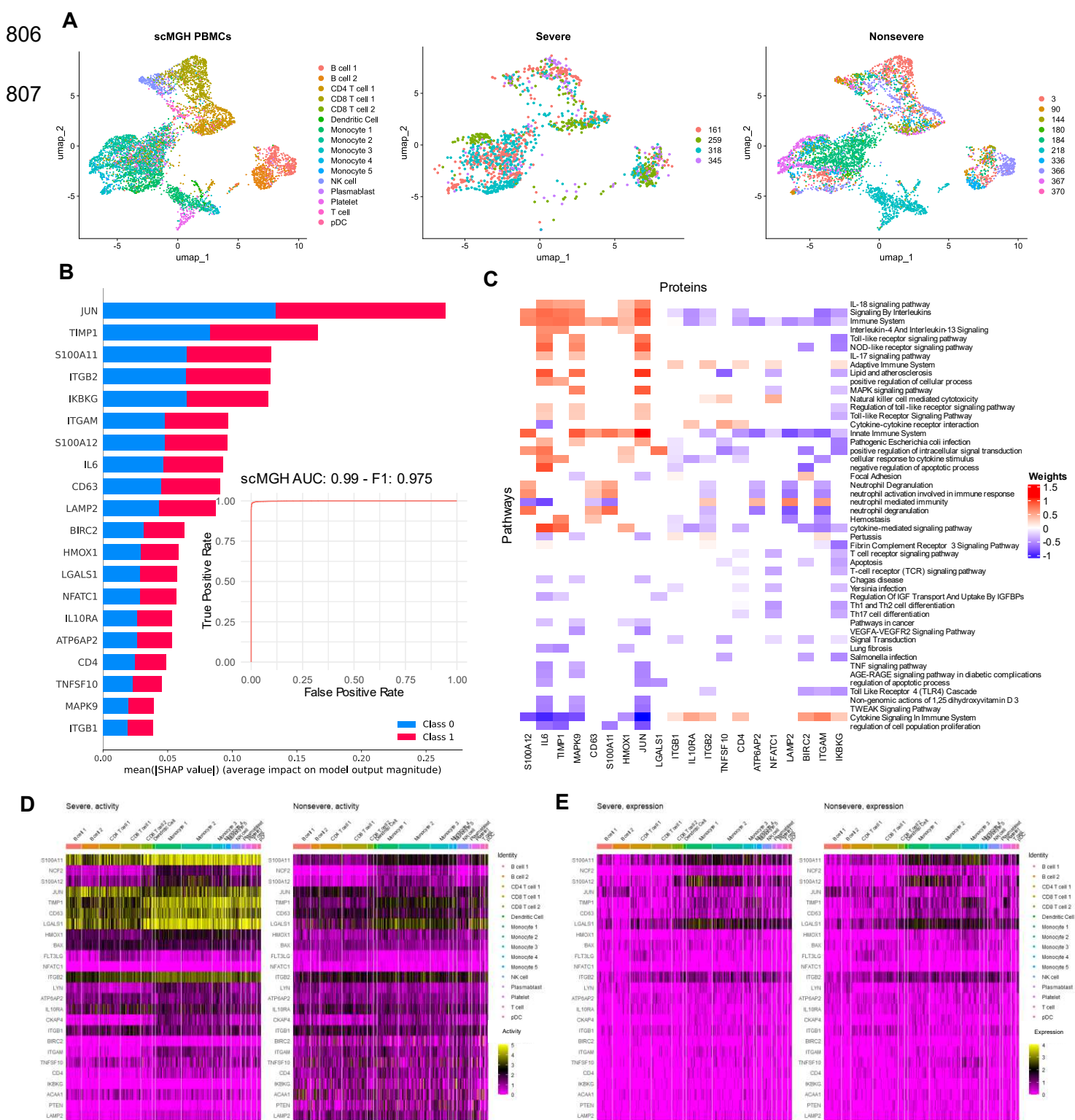


**Figure 5. APNet classifies severe COVID-19 cases across multi-omic studies. (A) scRNA-seq data from the Villani group for 14 MGH cases. (B-C) Bar plots for SHAP values and driver-pathway mapping from PASNet signifying the top-20 predictive drivers and their corresponding pathways, for the MGH plasma proteomic (training) / scRNA-seq (testing) experiment. Furthermore, the AUC and F1-score values are depicted. Class 0 refers to nonsevere and Class 1 refers to severe COVID-19 cases. (D-E) Heatmaps depicting the activity and the expression of predictive drivers from all the APNet experiments, across various PBMC cell types. The scMINER toolkit and visualisation performed the activity calculations were attained through Seurat. Only the predictive drivers with positive activity values are depicted.**

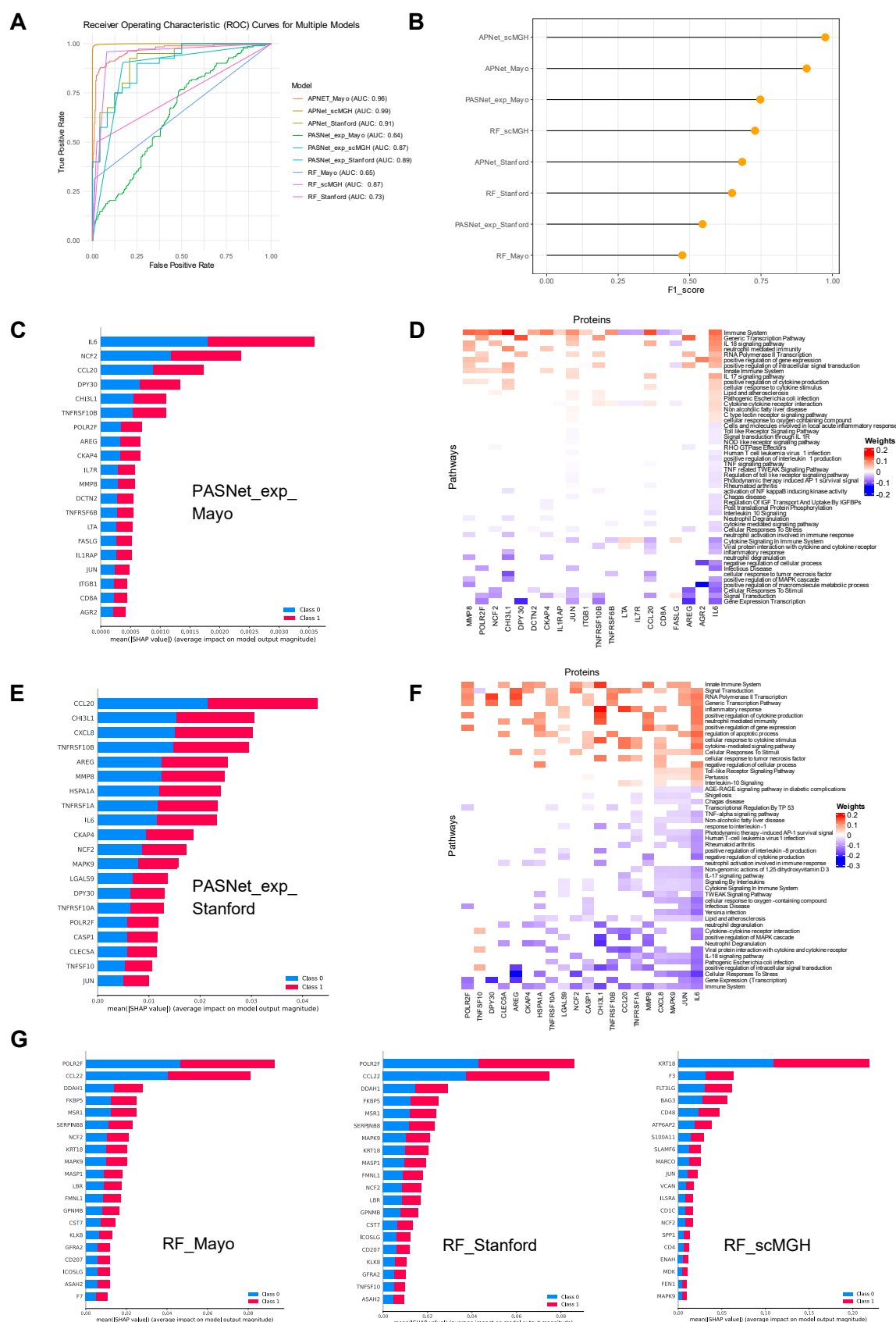


**Figure 6. APNet outperforms alternative ML/DL models in classifying severe and non-severe COVID-19 cases. (A)** ROC curves depicting the performance of APNet and alternative approaches in classifying severe from non-severe cases in respective experiments. Distinct AUC scores are referenced also. **(B)** Lollipop plot depicting the F1-scores from each model from (A). **(C-F)** Barplots with SHAP values for the top 20 most predictive plasma proteins of COVID-19 severity and protein-pathway mapping from PASNet-expression model for MGH-Mayo experiment (C-D) and MGH-Stanford experiment (E-F). **(G)** Barplots with SHAP values showing top 20 most predictive drivers of severity based on the Random Forest (RF) alternative model for the various classification experiments. Class 0 refers to non-severe and Class 1 refers to severe COVID-19 cases.

APNet uncovers predictive drivers of COVID-19 severity

809

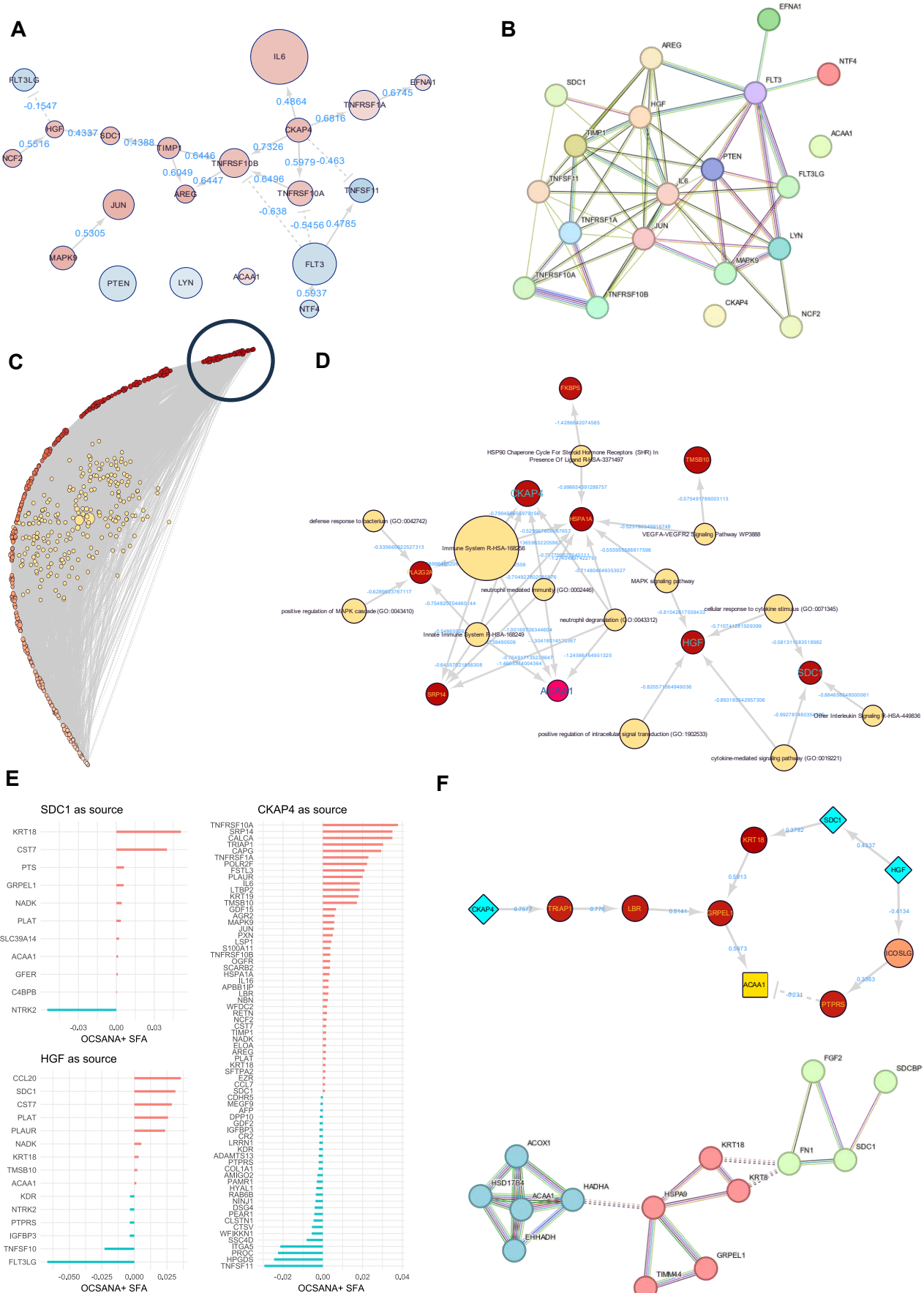


**Figure 7. APNet enables the assembly of complex graphs that can be leveraged to discover non-apparent connections of ACAA1 with other predictive drivers of COVID-19 severity. (A)** SJARACNe co-expression ( $\text{adj.pvalue} < 0.05$  for MI calculation) directed network from APNet's complex graph showing the interactions of the top 20 most predictive drivers of COVID-19 severity for the MGH-Mayo scenario. **(B)** STRINGdb network with (interaction score  $> 0.4$ ) for the same severity drivers. **(C)** APNet's complex graph after tSNE dimensionality reduction using the clusterMaker app in Cytoscape, based on the “liver” score from the TISSUES 2.0 database for each driver/node. The darkest colour denotes a higher liver-specific association. The most liver-specific cluster of drivers is designated within the circle (continue to next page...)

810

**Figure 7. APNet enables the assembly of complex graphs that can be leveraged to discover non-apparent connections of ACAA1 with other predictive drivers of COVID-19 severity (continued..) (D)** Part of APNet's complex graph showing highly liver-specific drivers and connected pathways with high prognostic significance, based on their PASNet weights. **(E)** Lollipop plots showing the SFA scores from the OCSANA+ app in Cytoscape in each node, after signal propagation from SDC1, CKAP4 and HGF on the entire APNet complex graph. **(F)** Part of APNet's complex graph showing shortest paths based on the PathLinker app in Cytoscape starting from CKAP4, SDC1 and HGF and extending towards ACAA1. Below, the STRINGdb equivalent PPI network (interaction score > 0.4) of the SDC1-KRT18-GRPEL1-ACAA1 path with intermediate nodes provided by STRINGdb, after k-means clustering.